

This is the accepted manuscript made available via CHORUS. The article has been published as:

Quantal diffusion description of multinucleon transfers in heavy-ion collisions

S. Ayik, B. Yilmaz, O. Yilmaz, and A. S. Umar

Phys. Rev. C **97**, 054618 — Published 29 May 2018

DOI: [10.1103/PhysRevC.97.054618](https://doi.org/10.1103/PhysRevC.97.054618)

Quantal Diffusion Description of Multi-Nucleon Transfers in Heavy-Ion Collisions

S. Ayik,^{1,*} B. Yilmaz,² O. Yilmaz,³ and A. S. Umar⁴

¹*Physics Department, Tennessee Technological University, Cookeville, TN 38505, USA*

²*Physics Department, Faculty of Sciences, Ankara University, 06100 Ankara, Turkey*

³*Physics Department, Middle East Technical University, 06800 Ankara, Turkey*

⁴*Department of Physics and Astronomy, Vanderbilt University, Nashville, TN 37235, USA*

(Dated: May 16, 2018)

Employing the stochastic mean-field (SMF) approach, we develop a quantal diffusion description of the multi-nucleon transfer in heavy-ion collisions at finite impact parameters. The quantal transport coefficients are determined by the occupied single-particle wave functions of the time-dependent Hartree-Fock equations. As a result, the primary fragment mass and charge distribution functions are determined entirely in terms of the mean-field properties. This powerful description does not involve any adjustable parameter, includes the effects of shell structure and is consistent with the fluctuation-dissipation theorem of the non-equilibrium statistical mechanics. As a first application of the approach, we analyze the fragment mass distribution in $^{48}\text{Ca} + ^{238}\text{U}$ collisions at the center-of-mass energy $E_{\text{c.m.}} = 193$ MeV and compare the calculations with the experimental data.

I. INTRODUCTION

The renewed interest in the study of ion-ion collisions involving heavy systems is driven partially by the search for new neutron rich nuclei. For this purpose, a number of experimental investigations of multi-nucleon transfer processes have been carried out in heavy-ion collision with actinide targets near barrier energies [1,2]. Collisions of heavy systems at low energies predominantly lead to dissipative deep-inelastic collisions and quasi-fission reactions. In dissipative collisions the part of the bombarding energy is converted into internal excitations and multi-nucleon transfer occurs between the projectile and target nuclei. In particular, the quasi-fission reactions of heavy-ions provide an important tool for massive mass transfer [2–22]. In quasi-fission colliding ions attach together for a long time but separate without going through a compound nucleus formation. During the long contact time a substantial nucleon exchange takes place between projectile and target nuclei. A number of models have been developed for the description of quasi-fission reaction mechanism in terms of multi-nucleon transfer process [23–26]. The time-dependent Hartree-Fock (TDHF) theory provides a microscopic alternative for describing heavy-ion reaction mechanism at low bombarding energies [27–29]. In recent years the TDHF approach has been extensively used to study the quasi-fission reactions [16,19,20,30–35].

The TDHF theory provides a good description for the average values of the collective reaction dynamics, however the approach is not able to describe the fluctuations of the collective dynamics. In TDHF studies it is possible to calculate the mean values of neutron and proton drifts. It is also possible to calculate fragment mass and charge distributions by the particle number projection approach [36–40]. But this description works best for few nucleon transfer, and therefore dispersions of distributions of multi-nucleon transfers are severely underestimated in dissipative collisions [41,42]. Much effort

has been devoted to improve the standard mean-field approximation by including fluctuation mechanism into the description. These include the Boltzmann-Langevin transport approach [43], the time-dependent random-phase approximation (TDRPA) approach of Balian and Vénéroni [44,45], the time-dependent generator coordinate method (TDGCM) [46], and the stochastic mean-field (SMF) approach [47]. The applications of time-dependent density matrix (TDDM) approach on reaction of heavy system have also been recently reported [48–50]. Here, we present applications of the SMF approach on multi-nucleon transfer reactions [51].

In essence there are two different mechanism for the dynamics of density fluctuations: (i) The collisional mechanism due to short-range two nucleon correlations, which is incorporated in to the Boltzmann-Langevin approach. This mechanism is important in nuclear collisions at bombarding energies per particle around the Fermi energy, but it does not have sizable effect at low energies. (ii) At low bombarding energies, near the Coulomb barrier, the long-range mean-field fluctuations originating from the fluctuations of the initial state becomes the dominant source for the dynamics of density fluctuations. In the SMF approach, these mean-field fluctuations are incorporated into the description of the initial state. The standard mean-field dynamics provides a deterministic description, in which a well specified initial conditions lead to a definite final state. In contrast, in the SMF approach the initial conditions are specified with a suitable distribution of the relevant degrees of freedom [47]. An ensemble of mean-field events are generated from the specified fluctuations of the initial state. In a number of studies, it has been demonstrated that the SMF provides a good approximation for nuclear dynamics including fluctuation mechanism of the collective motion [47,51–55]. For these low energy collisions the di-nuclear structure is largely maintained. In this case, it is possible to define macroscopic variables with the help of the window dynamics. The SMF approach gives rise to a Langevin description for the evolution of macroscopic variables [56,57] and provides a microscopic basis to calculate transport coefficients for the macroscopic variables. In the initial applications, this approach has been applied to the nucleon diffusion mecha-

* ayik@tntech.edu

nism in the semi-classical limit and by ignoring the memory effects [58–60]. In a recent work, from the SMF approach, we were able to deduce the quantal diffusion coefficients for nucleon exchange in the central collisions of heavy-ions. The quantal transport coefficients include the effect of shell structure, take into account the full geometry of the collision process, and incorporate the effect of Pauli blocking exactly. Recently, we applied the quantal diffusion approach and carried out calculations for the variance of neutron and proton distributions of the outgoing fragments in the central collisions of several symmetric heavy-ion systems at energies slightly below the fusion barriers [61]. In another work, we carried out quantal nucleon diffusion calculations and determined the primary fragment mass and charge distributions for the central collisions of $^{238}\text{U} + ^{238}\text{U}$ system [62].

In this work, we extend the diffusion description for collisions to incorporate finite impact parameters, and deduce quantal transport coefficients for the proton and neutron diffusion in heavy-ion collisions. Since the transport coefficients do not involve any fitting parameter, the description may provide a useful guidance for the experimental investigations of heavy neutron rich isotopes in the reaction mechanism. As a first application of the formalism, we carry out quantal nucleon diffusion calculations for $^{48}\text{Ca} + ^{238}\text{U}$ collisions at the center-of-mass energy $E_{\text{c.m.}} = 193$ MeV and determine the primary fragment mass distribution [1]. In section II, we present a brief description of the quantal nucleon diffusion mechanism based on the SMF approach. In section III, we present derivation of the quantal neutron and proton diffusion coefficients. The result of calculations for $^{48}\text{Ca} + ^{238}\text{U}$ collisions is reported in section IV, and conclusions are given in section V.

II. QUANTAL NUCLEON DIFFUSION MECHANISM

We consider collisions of heavy-ions in which the di-nuclear structure is maintained, such as in the deep-inelastic collision or quasi-fission reactions. In this case, when the ions start to touch a window is formed between the colliding ions. In collisions with finite impact parameters, the window dynamics is more complex than the central collisions. In order to incorporate the vectorial character of the nucleon flux across the window as well as the rotation dynamics of the di-nuclear complex, we derive the neutron and proton diffusion coefficients, and determine the derivatives of the drift coefficients in an analogous way to the central collisions discussed in Refs. [61,62]. We represent the reaction plane in a collision by (x, y) -plane, where x -axis is taken in the beam direction in the c.m. frame of colliding ions. Window plane is perpendicular to the symmetry axis and its orientation is specified by

$$y - y_0(t) = -[x - x_0(t)] \cot \theta(t) \quad (1)$$

In this expression, $x_0(t)$ and $y_0(t)$ denote the coordinates of the window center relative to the origin of the c.m. frame, $\theta(t)$ is the smaller angle between the orientation of the symmetry axis and the beam direction. For each impact parameter b , as

described in Appendix A, by employing the TDHF solutions, it is possible to determine time evolution of the rotation angle $\theta(t)$ of the symmetry axis. The coordinates $x_0(t)$ and $y_0(t)$ of the center point of the window are located at the center of the minimum density slice on the neck between the colliding ions. In the following, all quantities are calculated for a given impact parameter b or the initial orbital angular momentum l , but for the purpose of clarity of certain expressions, we do not attach the impact parameter or the angular momentum label to the quantities.

In the SMF approach, the collision dynamics is analyzed in terms of an ensemble of mean-field events. In each event, we choose the neutron $N_1^\lambda(t)$ and proton $Z_1^\lambda(t)$ numbers of the projectile-like fragments as independent variables, where λ denotes the event label. The neutron and proton numbers can be determined at each instant by integrating the neutron and proton densities over the projectile-like side of the window for each event λ by employing the expression,

$$\begin{pmatrix} N_1^\lambda(t) \\ Z_1^\lambda(t) \end{pmatrix} = \int d^3r \Theta[(x - x_0) \cos \theta + (y - y_0) \sin \theta] \times \begin{pmatrix} \rho_n^\lambda(\vec{r}, t) \\ \rho_p^\lambda(\vec{r}, t) \end{pmatrix}. \quad (2)$$

Here, the quantity

$$\rho_\alpha^\lambda(\vec{r}, t) = \sum_{ij \in \alpha} \Phi_{ij}^{*\alpha}(\vec{r}, t; \lambda) \rho_{ji}^\lambda \Phi_i^\alpha(\vec{r}, t; \lambda) \quad (3)$$

denotes the neutron and proton number densities for the event λ of the ensemble of the single-particle density matrices. Here and in the rest of the article, we use the notation $\alpha = n, p$ for the proton and neutron labels. According to the main postulate of the SMF approach, the elements of the initial density matrix have uncorrelated Gaussian distributions with the mean values $\rho_{ji}^\lambda = \delta_{ji} n_j$ and the second moments determined by,

$$\overline{\delta \rho_{ji}^\lambda \delta \rho_{i'j'}^\lambda} = \frac{1}{2} \delta_{ii'} \delta_{jj'} [n_i(1 - n_j) + n_j(1 - n_i)] \quad (4)$$

where n_j are the average occupation numbers of the single-particle wave functions at the initial state. At zero initial temperature, the occupation numbers are zero or one, at finite initial temperatures the occupation numbers are given by the Fermi-Dirac functions. Here and below, the bar over the quantity indicates the average over the generated ensemble. In each event the complete set of single-particle wave functions is determined by the TDHF equations with the self-consistent Hamiltonian $h(\rho^\lambda)$ of that event,

$$i\hbar \frac{\partial}{\partial t} \Phi_i^\alpha(\vec{r}, t; \lambda) = h(\rho^\lambda) \Phi_i^\alpha(\vec{r}, t; \lambda). \quad (5)$$

The rate of changes the neutron and the proton numbers of the projectile-like fragment are given by,

$$\begin{aligned} \frac{d}{dt} \begin{pmatrix} N_1^\lambda(t) \\ Z_1^\lambda(t) \end{pmatrix} &= \int d^3r \delta(x') \dot{x}' \begin{pmatrix} \rho_n^\lambda(\vec{r}, t) \\ \rho_p^\lambda(\vec{r}, t) \end{pmatrix} \\ &+ \int d^3r \Theta(x') \frac{\partial}{\partial t} \begin{pmatrix} \rho_n^\lambda(\vec{r}, t) \\ \rho_p^\lambda(\vec{r}, t) \end{pmatrix}, \quad (6) \end{aligned}$$

where $x' = \hat{e} \cdot (\vec{r} - \vec{r}_0)$, $\dot{x}' = \vec{\theta} \cdot [\hat{e} \times (\vec{r} - \vec{r}_0)] - \hat{e} \cdot \dot{\vec{r}}_0$ with \vec{r}_0 and $\dot{\vec{r}}_0$ as the position and velocity vectors of the center of the window plane in the c.m. frame. Here and below, \hat{e} denotes the unit vector along the symmetry axis with components $\hat{e}_x = \cos \theta$ and $\hat{e}_y = \sin \theta$. Using the continuity equation,

$$\frac{\partial}{\partial t} \rho_\alpha^\lambda(\vec{r}, t) = -\vec{\nabla} \cdot \vec{j}_\alpha^\lambda(\vec{r}, t), \quad (7)$$

we can express Eq. (6) as,

$$\begin{aligned} \frac{d}{dt} \begin{pmatrix} N_1^\lambda(t) \\ Z_1^\lambda(t) \end{pmatrix} &= \int d^3r g(x') \begin{pmatrix} x' \rho_n^\lambda(\vec{r}, t) + \hat{e} \cdot \vec{j}_n^\lambda(\vec{r}, t) \\ x' \rho_p^\lambda(\vec{r}, t) + \hat{e} \cdot \vec{j}_p^\lambda(\vec{r}, t) \end{pmatrix} \\ &= \begin{pmatrix} v_n^\lambda(t) \\ v_p^\lambda(t) \end{pmatrix}. \end{aligned} \quad (8)$$

In this expression and below, for convenience, we replace the delta function $\delta(x)$ by a Gaussian $g(x) = (1/\kappa\sqrt{2\pi}) \exp(-x^2/2\kappa^2)$ which behaves almost like delta function for sufficiently small κ . In the numerical calculations dispersion of the Gaussian is taken in the order of the lattice size $\kappa = 1.0$ fm. The right side of Eq. (8) defines the drift coefficients $v_\alpha^\lambda(t)$ for the neutrons and the protons for the event λ . In the SMF approach the current density vector is given by,

$$\begin{aligned} \vec{j}_\alpha^\lambda(\vec{r}, t) &= \frac{\hbar}{2im} \sum_{ij \in \alpha} \left[\Phi_j^{*\alpha}(\vec{r}, t; \lambda) \vec{\nabla} \Phi_i^\alpha(\vec{r}, t; \lambda) \right. \\ &\quad \left. - \Phi_i^\alpha(\vec{r}, t; \lambda) \vec{\nabla} \Phi_j^{*\alpha}(\vec{r}, t; \lambda) \right] \rho_{ji}^\lambda \\ &= \frac{\hbar}{m} \sum_{ij \in \alpha} \text{Im} \left(\Phi_j^{*\alpha}(\vec{r}, t; \lambda) \vec{\nabla} \Phi_i^\alpha(\vec{r}, t; \lambda) \rho_{ji}^\lambda \right). \end{aligned} \quad (9)$$

Equation (8) provides a Langevin description for the stochastic evolution the neutron and the proton numbers of the projectile-like fragments. Drift coefficients $v_\alpha^\lambda(t)$ fluctuate from event to event due to stochastic elements of the initial density matrix ρ_{ji}^λ and also due to the different sets of the wave functions in different events. As a result, there are two sources for fluctuations of the nucleon drift coefficients: (i) fluctuations those arise from the different set of single-particle wave functions in each event, and (ii) the explicit fluctuations $\delta v_p^\lambda(t)$ and $\delta v_n^\lambda(t)$ arising from the stochastic part of proton and neutron currents.

A. Mean neutron and proton drift path

Equations for the mean values of proton $Z_1(t) = \overline{Z_1^\lambda(t)}$ and neutron $N_1(t) = \overline{N_1^\lambda(t)}$ numbers of the projectile-like fragments are obtained by taking the ensemble averaging of the Langevin equation (8). For small amplitude fluctuations, and using the fact that average values of density matrix elements are given by the average occupation numbers as $\overline{\rho_{ji}^\lambda} = \delta_{jinj}$, we obtain the usual mean-field result given by the TDHF

equations,

$$\begin{aligned} \frac{d}{dt} \begin{pmatrix} N_1(t) \\ Z_1(t) \end{pmatrix} &= \int d^3r g(x') \begin{pmatrix} x' \rho_n(\vec{r}, t) + \hat{e} \cdot \vec{j}_n(\vec{r}, t) \\ x' \rho_p(\vec{r}, t) + \hat{e} \cdot \vec{j}_p(\vec{r}, t) \end{pmatrix} \\ &= \begin{pmatrix} v_n(t) \\ v_p(t) \end{pmatrix}. \end{aligned} \quad (10)$$

Here, the mean values of the densities and the currents densities of neutron and protons are given by,

$$\rho_\alpha(\vec{r}, t) = \sum_{h \in \alpha} \Phi_h^{*\alpha}(\vec{r}, t) \Phi_h^\alpha(\vec{r}, t) \quad (11)$$

and

$$\vec{j}_\alpha(\vec{r}, t) = \frac{\hbar}{m} \sum_{h \in \alpha} \text{Im} \left(\Phi_h^{*\alpha}(\vec{r}, t) \vec{\nabla} \Phi_h^\alpha(\vec{r}, t) \right), \quad (12)$$

where the summation h runs over the occupied states originating both from the projectile and the target nuclei. The drift coefficients $v_p(t)$ and $v_n(t)$ denote the net proton and neutron currents across the window.

Since the uranium nucleus has large quadrupole deformation, the collision takes place in many different geometries. In this work, we observe that the dominant contribution to the fragment distributions in the $^{48}\text{Ca} + ^{238}\text{U}$ collisions at $E_{\text{c.m.}} = 193$ MeV, reported in [1], are coming from the tip geometry of the uranium nucleus. Therefore in analyzing the measured data we incorporate only collisions involving the tip configuration of the uranium. Figure 1 illustrate the density profile of the $^{48}\text{Ca} + ^{238}\text{U}$ collisions in the tip geometry of the uranium with $E_{\text{c.m.}} = 193$ MeV at an impact parameter $b = 2.8$ fm, or equivalently at the initial orbital angular momentum $\ell = 54\hbar$ at several times during the collision. This computation and all other numerical computation in this work are carried out by employing 3D TDHF program of Umar *et al.* [63,64]. The SLy4d Skyrme interaction [65,66] is used. Figure 2 illustrate neutron and proton drift coefficients at the same energy and the same impact parameter. The fluctuations of the drift coefficients as function of time is a result of the shell structure of the population of different nuclei during the evolution of the projectile-like and target-like nuclei. Even the more interesting presentation of the results of the mean-field evolution in the tip geometry is presented in Fig. 3 at the same c.m. energy for a few different impact parameters. This figure shows the mean drift-path of di-nuclear system in the (N, Z) plane. After touching, we observe a rapid charge equilibration, which is not very visible due to the fact that the colliding nuclei and the composite system have nearly same charge asymmetry. After touching, di-nuclear system drift toward symmetry along the valley of the beta stability line nearly the similar manner in collisions for different impact parameters. The neutron and proton numbers of the symmetric equilibrium state are $N_0 = (N_P + N_T)/2 = 87$ and $Z_0 = (Z_P + Z_T)/2 = 56$. As seen from the mean drift path, during the mean evolution, the system separate before reaching the symmetric equilibrium state.

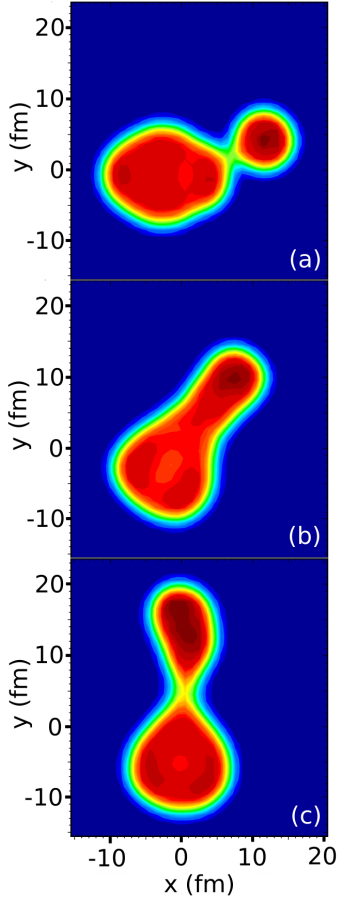


FIG. 1. (color online) The density profile of the $^{48}\text{Ca} + ^{238}\text{U}$ collisions in the tip geometry of the uranium nucleus at $E_{\text{c.m.}} = 193$ MeV and at impact parameter $b = 2.8$ fm, or equivalently the initial orbital angular momentum $\ell = 54\hbar$, at times $t = 300$ fm/c (a), $t = 1170$ fm/c (b) and $t = 2070$ fm/c (c).

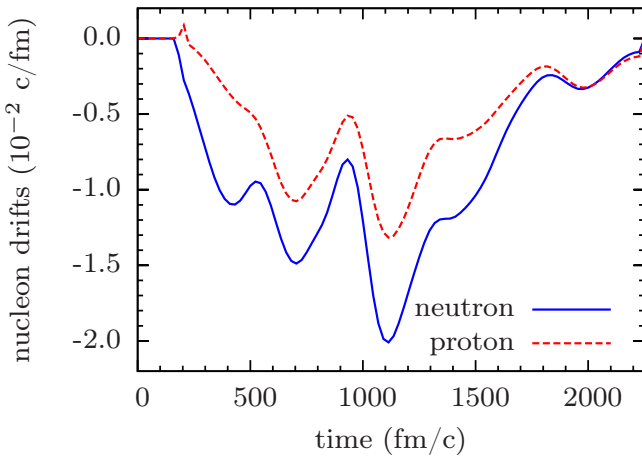


FIG. 2. (color online) The neutron and proton drift coefficient the $^{48}\text{Ca} + ^{238}\text{U}$ collisions in the tip geometry of the uranium nucleus at $E_{\text{c.m.}} = 193$ MeV at an impact parameter $b = 2.8$ fm or equivalently at the initial orbital angular momentum $\ell = 54\hbar$.

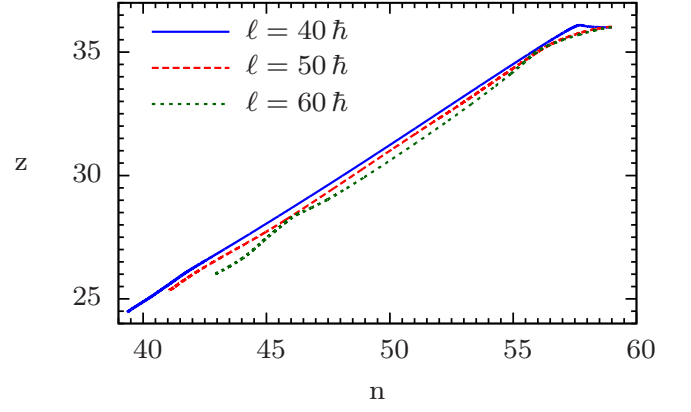


FIG. 3. (color online) The neutron and proton mean-drift path in the (N, Z) plane, in the $^{48}\text{Ca} + ^{238}\text{U}$ collisions in the tip geometry of the uranium at $E_{\text{c.m.}} = 193$ MeV at the impact parameters $b = 2.1$ fm, $b = 2.6$ fm and $b = 3.1$ fm or equivalently at the initial angular momentum $\ell = 40\hbar$, $\ell = 50\hbar$ and $\ell = 60\hbar$. Here $n = N_0 - N_1$ and $z = Z_0 - Z_1$, with N_1 and Z_1 indicating the light fragments.

B. Co-variances of fragment charge and mass distributions

Our task is to evaluate the fluctuations of the neutron and proton numbers around their mean values. For this purpose, we linearize the Langevin Eq. (8) around their mean values $Z_1(t)$ and $N_1(t)$. There are two different sources of the fluctuations. First contribution arises from the different set of wave functions in different events. In the leading order, we can express this effect as deviations of the drift coefficients from their mean values in terms of fluctuations in neutron and proton numbers. The second contribution arises from the initial fluctuations of the elements of the density matrix. As a result the linearized form of the Langevin Eq. (8) becomes,

$$\frac{d}{dt} \begin{pmatrix} Z_1^\lambda(t) \\ N_1^\lambda(t) \end{pmatrix} = \begin{pmatrix} \frac{\partial v_p}{\partial Z_1} (Z_1^\lambda - Z_1) + \frac{\partial v_p}{\partial N_1} (N_1^\lambda - N_1) \\ \frac{\partial v_n}{\partial Z_1} (Z_1^\lambda - Z_1) + \frac{\partial v_n}{\partial N_1} (N_1^\lambda - N_1) \end{pmatrix} + \begin{pmatrix} \delta v_p^\lambda(t) \\ \delta v_n^\lambda(t) \end{pmatrix}. \quad (13)$$

The linear limit provides a good approximation for small amplitude fluctuations and it becomes even better if the fluctuations are nearly harmonic around the mean values. The derivatives of drift coefficients are evaluated on the mean trajectory and the quantities $\delta v_\alpha^\lambda(t)$ denote the stochastic part of drift coefficients given by,

$$\delta v_\alpha^\lambda(t) = \int d^3r g(x') \left(\dot{x}' \delta \rho_\alpha^\lambda(\vec{r}, t) + \hat{e} \cdot \delta \vec{j}_\alpha^\lambda(\vec{r}, t) \right), \quad (14)$$

with the fluctuating neutron and proton current densities

$$\delta \vec{j}_\alpha^\lambda(\vec{r}, t) = \frac{\hbar}{m} \sum_{ij \in \alpha} \text{Im} \left(\Phi_j^{*\alpha}(\vec{r}, t) \vec{\nabla} \Phi_i^\alpha(\vec{r}, t) \delta \rho_{ji}^\lambda \right), \quad (15)$$

and the fluctuating neutron and proton number densities

$$\delta \rho_\alpha^\lambda(\vec{r}, t) = \sum_{ij \in \alpha} \Phi_j^{*\alpha}(\vec{r}, t) \delta \rho_{ji}^\lambda \Phi_i^\alpha(\vec{r}, t). \quad (16)$$

The variances and the co-variance of neutron and proton distribution of projectile fragments are defined as $\sigma_{NN}^2(t) = \overline{(N_1^\lambda - N_1)^2}$, $\sigma_{ZZ}^2(t) = \overline{(Z_1^\lambda - Z_1)^2}$, and $\sigma_{NZ}^2(t) = \overline{(N_1^\lambda - N_1)(Z_1^\lambda - Z_1)}$. Multiplying both side of Langevin equations (13) by $N_1^\lambda - N_1$ and $Z_1^\lambda - Z_1$, and taking the ensemble average, we find evolution of the co-variances are specified by the following set of coupled differential equations [67,68],

$$\frac{\partial}{\partial t} \sigma_{NN}^2 = 2 \frac{\partial v_n}{\partial N_1} \sigma_{NN}^2 + 2 \frac{\partial v_n}{\partial Z_1} \sigma_{NZ}^2 + 2D_{NN}, \quad (17)$$

$$\frac{\partial}{\partial t} \sigma_{ZZ}^2 = 2 \frac{\partial v_p}{\partial Z_1} \sigma_{ZZ}^2 + 2 \frac{\partial v_p}{\partial N_1} \sigma_{NZ}^2 + 2D_{ZZ}, \quad (18)$$

and

$$\frac{\partial}{\partial t} \sigma_{NZ}^2 = \frac{\partial v_p}{\partial N_1} \sigma_{NN}^2 + \frac{\partial v_n}{\partial Z_1} \sigma_{ZZ}^2 + \sigma_{NZ}^2 \left(\frac{\partial v_p}{\partial Z_1} + \frac{\partial v_n}{\partial N_1} \right). \quad (19)$$

In these expressions, D_{NN} and D_{ZZ} denote the neutron and proton quantal diffusion coefficients which are discussed in the next section. It is well know that the Langevin Eq. (13) is equivalent to the Fokker-Planck equation for the distribution function $P_b(N, Z, t)$ of the macroscopic variables [69]. In the tip geometry there is a cylindrical symmetry for the distribution function for each impact parameter. As a result, for each impact parameter b (or the initial orbital angular momentum ℓ), the proton and neutron distribution function $P_b(N, Z, t)$ of the project-like or the target-like fragments is a correlated Gaussian function described by the mean values and the co-variances as,

$$P_b(N, Z, t) = \frac{1}{2\pi\sigma_{NN}(b)\sigma_{ZZ}(b)\sqrt{1-\rho_b^2}} \exp(-C_b). \quad (20)$$

Here, the argument of the exponent C_b for each impact parameter is given by

$$C_b = \frac{1}{2(1-\rho_b^2)} \left[\left(\frac{Z - Z_b}{\sigma_{ZZ}(b)} \right)^2 - 2\rho_b \left(\frac{Z - Z_b}{\sigma_{ZZ}(b)} \right) \left(\frac{N - N_b}{\sigma_{NN}(b)} \right) + \left(\frac{N - N_b}{\sigma_{NN}(b)} \right)^2 \right], \quad (21)$$

with $\rho_b = \sigma_{NZ}^2(b)/\sigma_{ZZ}(b)\sigma_{NN}(b)$. The mean values $N_b = \bar{N}_b$, $Z_b = \bar{Z}_b$ denote the mean neutron and proton numbers of the target-like or project-like fragments. The set of coupled Eqs. (17-19) for co-variances are familiar from the phenomenological nucleon exchange model, and they were derived from the Fokker-Planck equation for the fragment neutron and proton distributions in the deep-inelastic heavy-ion collisions [67,68]. Equation (20) determines the joint probability distribution at a given impact parameter. Then, it is possible to calculate the cross-section $\sigma(N, Z)$ for production of nuclei with neutron and proton numbers by integrating the probability distributions over the range of the impact parameters corresponds to the experimental data as,

$$\sigma(N, Z) = \int_{b_1}^{b_2} 2\pi b P_b(N, Z) db, \quad (22)$$

where $P_b(N, Z)$ denotes the distribution functions at the separation instant of the fragments. Distribution $P_b(A - A_b)$ of the mass number of the fragments is obtained by substituting $Z = A - N$ in $P_b(N, Z)$ and integrating over N . For a given impact parameter this yields a Gaussian function for the mass number distribution of the target-like or projectile-like fragments,

$$P_b(A - A_b) = \frac{1}{\sqrt{2\pi}\sigma_{AA}(b)} \exp \left[-\frac{1}{2} \left(\frac{A - A_b}{\sigma_{AA}(b)} \right)^2 \right], \quad (23)$$

where $A_b = N_b + Z_b$ is the mean value of the mass number and the variance given by $\sigma_{AA}^2(b) = \sigma_{NN}^2(b) + \sigma_{ZZ}^2(b) + 2\sigma_{NZ}^2(b)$. The cross-section for production of nuclei with a mass number $A = N + Z$ is calculated in the similar manner to Eq. (22).

III. TRANSPORT COEFFICIENTS

A. Quantal Diffusion Coefficients

Stochastic part of the drift coefficients $\delta v_p^\lambda(t)$ and $\delta v_n^\lambda(t)$ are specified by uncorrelated Gaussian distributions. Stochastic drift coefficients have zero mean values $\overline{\delta v_p^\lambda(t)} = 0$, $\overline{\delta v_n^\lambda(t)} = 0$ and the associated correlation functions [56,57],

$$\int_0^t dt' \overline{\delta v_\alpha^\lambda(t) \delta v_\alpha^\lambda(t')} = D_{\alpha\alpha}(t), \quad (24)$$

determine the diffusion coefficients $D_{\alpha\alpha}(t)$ for proton and neutron transfers. As seen from Eq. (14), there are two different contribution to the stochastic part of the drift coefficients: (i) density fluctuations in vicinity of the rotating window plane which involves collective velocity of the window and (ii) current density fluctuation across the rotating window. Since nucleon flow velocity through the window is much larger than the collective velocity of the window, the current density fluctuations current make the dominant contribution. Therefore in our analysis, we retain only the current density fluctuations in the stochastic part of the drift coefficients,

$$\delta v_\alpha^\lambda(t) = \frac{\hbar}{m} \int d^3r g(x') \times \sum_{ij \in \alpha} \text{Im} \left(\Phi_j^{*\alpha}(\vec{r}, t) \hat{e} \cdot \vec{\nabla} \Phi_i^\alpha(\vec{r}, t) \delta \rho_{ji}^\lambda \right). \quad (25)$$

Furthermore, in the stochastic part of the drift coefficients, we impose a physical constraint on the summations of single-particle states. The transitions among the single particle states originating from the projectile or target nuclei do not contribute to nucleon exchange mechanism. Therefore in Eq. (25), we restrict summation as follows: when the summation $i \in T$ runs over the states originating from the target nucleus, the summation $j \in P$ runs over the states originating from the projectile, and vice versa. Using the main postulate of the SMF approach given by Eq. (4), we can calculate the correlation functions of the stochastic part of the drift coefficients. At zero temperature, since the average occupation

factor are zero or one, we find the correlation functions is expressed as,

$$\overline{\delta v_{\alpha}^{\lambda}(t) \delta v_{\alpha}^{\lambda}(t')} = \text{Re} \left(\sum_{p \in P, h \in T} A_{ph}^{\alpha}(t) A_{ph}^{*\alpha}(t') + \sum_{p \in T, h \in P} A_{ph}^{\alpha}(t) A_{ph}^{*\alpha}(t') \right). \quad (26)$$

Here, and below, p and h indices denote the particle and hole states originating from the projectile and target, and the matrix elements are given by,

$$A_{ph}^{\alpha}(t) = \frac{\hbar}{2m} \int d^3 r g(x') \left(\Phi_p^{*\alpha}(\vec{r}, t) \hat{e} \cdot \vec{\nabla} \Phi_h^{\alpha}(\vec{r}, t) - \Phi_h^{\alpha}(\vec{r}, t) \hat{e} \cdot \vec{\nabla} \Phi_p^{*\alpha}(\vec{r}, t) \right). \quad (27)$$

We note that employing a partial integration, we can put this expression in the following form,

$$A_{ph}^{\alpha}(t) = \frac{\hbar}{m} \int d^3 r g(x') \Phi_p^{*\alpha}(\vec{r}, t) \times \left(\hat{e} \cdot \vec{\nabla} \Phi_h^{\alpha}(\vec{r}, t) - \frac{x'}{2\kappa^2} \Phi_h^{\alpha}(\vec{r}, t) \right). \quad (28)$$

In order to evaluate the correlation function Eq. (26) of the stochastic drift coefficient, we introduce the following approximate treatment. In the first term of the right hand side of Eq. (26), we add and subtract the hole contributions to give,

$$\sum_{p \in P, h \in T} A_{ph}^{\alpha}(t) A_{ph}^{*\alpha}(t') = \sum_{a \in P, h \in T} A_{ah}^{\alpha}(t) A_{ah}^{*\alpha}(t') - \sum_{h' \in P, h \in T} A_{h'h}^{\alpha}(t) A_{h'h}^{*\alpha}(t'). \quad (29)$$

Here, the summation a run over the complete set of states originating from the projectile. In the first term, we cannot use the closure relation to eliminate the complete set of single-particle states, because the wave functions are evaluated at different times. However, we note that the time-dependent single-particle wave functions during short time intervals exhibit nearly a diabatic behavior [70]. We introduce, during short time $\tau = t - t'$ evolution, in the order of the correlation time, a diabatic approximation into the time dependent wave-functions by shifting the time backward (or forward) according to [61,62],

$$\Phi_a(\vec{r}, t') \approx \Phi_a(\vec{r} - \vec{u}\tau, t). \quad (30)$$

where \vec{u} denotes a suitable flow velocity of nucleons through the window. Now, we can employ the closure relation to obtain,

$$\sum_a \Phi_a^*(\vec{r}_1, t) \Phi_a(\vec{r}_2 - \vec{u}\tau, t) = \delta(\vec{r}_1 - \vec{r}_2 + \vec{u}\tau), \quad (31)$$

where, the summation a runs over the complete set of states originating from target or projectile, and the closure relation is valid for each set of the spin-isospin degrees of freedom.

The flow velocity $\vec{u}(\vec{R}, T)$ may depend on the mean position $\vec{R} = (\vec{r}_1 + \vec{r}_2)/2$ and the time mean $T = (t + t')/2$. Employing the closure relation in the first term of the right hand side of Eq. (29), we find

$$\sum_{a \in P, h \in T} A_{ah}^{\alpha}(t) A_{ah}^{*\alpha}(t') = \sum_{h \in T} \int d^3 r_1 d^3 r_2 \delta(\vec{r}_1 - \vec{r}_2 + \vec{u}_h \tau) \times W_h^{\alpha}(\vec{r}_1, t) W_h^{*\alpha}(\vec{r}_2, t'). \quad (32)$$

The closure relation in Eq. (31) is valid for any choice of the flow velocity. The most suitable choice is the flow velocity of the hole state $\vec{u}_h(\vec{r}, T)$ in each term in the summation, which is taken in this expression. In this manner the complete set of single-particle states is eliminated and the calculations of the quantal diffusion coefficients are greatly simplified. In fact, in order to calculate this expression, we only need the hole states originating from target which are provided by the TDHF description. The local flow velocity of each wave-function is specified by the usual expression of the current density divided by the particle density as given in Eq. (B8) in Appendix B. The quantity $W_h^{\alpha}(\vec{r}_1, t)$ is given by,

$$W_h^{\alpha}(\vec{r}_1, t) = \frac{\hbar}{m} g(x'_1) \times \left(\hat{e} \cdot \vec{\nabla}_1 \Phi_h^{\alpha}(\vec{r}_1, t) - \frac{x'_1}{2\kappa^2} \Phi_h^{\alpha}(\vec{r}_1, t) \right), \quad (33)$$

and $W_h^{*\alpha}(\vec{r}_2, t')$ is given by a similar expression. A detailed analysis of Eq. (32) is presented in Appendix B. The result of this analysis as given by Eq. (B19) is,

$$\sum_{a \in P, h \in T} A_{ah}^{\alpha}(t) A_{ah}^{*\alpha}(t') = \int d^3 r \tilde{g}(x') G_T(\tau) \times J_{\perp, \alpha}^T(\vec{r}, t - \tau/2). \quad (34)$$

Here $J_{\perp, \alpha}^T(\vec{r}, t - \tau/2)$ represents the sum of the magnitude of current densities perpendicular to the window due to the each wave functions originating from target,

$$J_{\perp, \alpha}^T(\vec{r}, t - \tau/2) = \frac{\hbar}{m} \sum_{h \in T} \left| \text{Im} [\Phi_h^{*\alpha}(\vec{r}, t - \tau/2) \times (\hat{e} \cdot \vec{\nabla} \Phi_h^{\alpha}(\vec{r}, t - \tau/2))] \right|. \quad (35)$$

The quantity $G_T(\tau)$ is given by Eq. (B20), and it is the average value of the memory kernels $G_T^h(\tau)$ of Eq. (B13). It is possible to carry out a similar analysis in the second term in the right side of Eq. (13) to give,

$$\sum_{a \in T, h \in P} A_{ah}^{\alpha}(t) A_{ah}^{*\alpha}(t') = \int d^3 r \tilde{g}(x') G_P(\tau) \times J_{\perp, \alpha}^P(\vec{r}, t - \tau/2). \quad (36)$$

In a similar manner, $J_{\perp, \alpha}^P(\vec{r}, t - \tau/2)$ is determined by the sum of the magnitude of the current densities due wave functions originating from projectile. In Eq. (35) and Eq. (36) we use lower case \vec{r} instead of capital letter. As a result, the quantal

expressions of the proton and neutron diffusion coefficients takes the form,

$$D_{\alpha\alpha}(t) = \int_0^t d\tau \int d^3r \tilde{g}(x') [G_T(\tau) J_{\perp,\alpha}^T(\vec{r}, t - \tau/2) + G_P(\tau) J_{\perp,\alpha}^P(\vec{r}, t - \tau/2)] - \int_0^t d\tau \text{Re} \left(\sum_{h' \in P, h \in T} A_{h'h}^\alpha(t) A_{h'h}^{*\alpha}(t - \tau) + \sum_{h' \in T, h \in P} A_{h'h}^\alpha(t) A_{h'h}^{*\alpha}(t - \tau) \right). \quad (37)$$

These quantal expressions for the nucleon diffusion coefficients for heavy-ion collisions at finite impact parameters provide an extension of the result published in [62] for the central collisions. In general, we observe that there is a close analogy between the quantal expression and the classical diffusion coefficient in a random walk problem [56,57,71]. It is important to note that the quantal diffusion coefficients are entirely determined in terms of the occupied single-particle wave functions obtained from the TDHF solutions.

In our previous investigations we estimated the memory time of the average memory kernel $G_P(\tau)$ given by Eq. (B20) and similarly $G_T(\tau)$ [61,62]. We find that the average memory times $\tau_T = \tau_P \approx 25$ fm/c are much shorter than the typical interaction times which are around 1000 fm/c. Therefore, we can neglect the memory effect in the first term of the diffusion coefficients. For the same reason, memory effect is not very effective in the Pauli blocking terms in Eq. (37) as well, however in the calculations we keep the memory integrals in these terms. As an example, Fig. 4 shows the neutron and proton diffusion coefficients as a function of time in the $^{48}\text{Ca} + ^{238}\text{U}$ collisions in the tip geometry of the uranium at $E_{\text{c.m.}} = 193$ MeV and impact parameter $b = 2.8$ fm, or equivalently at the initial orbital angular momentum $\ell = 54\hbar$. As seen from the figure, neutron diffusion coefficient is nearly a factor of two larger than the proton diffusion coefficient.

B. Derivatives of drift coefficients

In order to determine the co-variances from Eqs. (17-19), in addition to the diffusion coefficients D_{ZZ} and D_{NN} , we need to know the rate of change of drift coefficients in the vicinity of their mean values. In order to calculate rates of change of the drift coefficients, we should calculate neighboring events in the vicinity of the mean-field path. Here, instead of such a detailed description, in order to determine the derivatives of the drift coefficients, we employ the fluctuation-dissipation theorem, which provides a general relation between the diffusion and drift coefficients in the transport mechanism of the relevant collective variables as often used in the phenomenological approaches [71,72]. Proton and neutron diffusion in the N-Z plane are driven in a correlated manner by the potential energy surface of the di-nuclear system. As a consequence of the symmetry energy, the diffusion in the direction perpendicular to the mean-drift path (the beta stability valley) takes

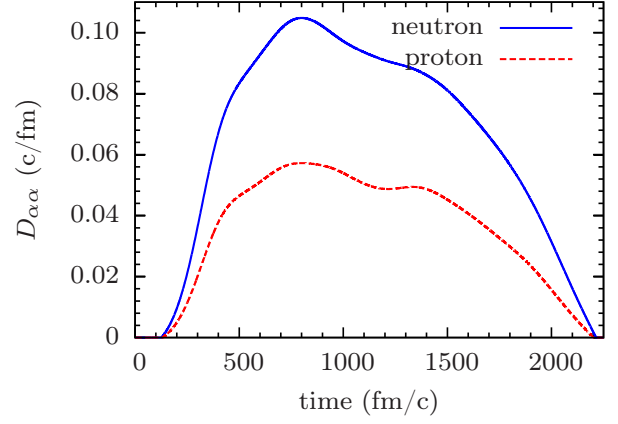


FIG. 4. (color online) The neutron and proton diffusion coefficients as a function of time in the $^{48}\text{Ca} + ^{238}\text{U}$ collisions in the tip geometry of the uranium at $E_{\text{c.m.}} = 193$ MeV and impact parameter $b = 2.8$ fm, or equivalently at the initial orbital angular momentum $\ell = 54\hbar$.

place rather rapidly leading to a fast equilibration of the charge asymmetry, and the diffusion continues rather slowly along the beta-stability valley. In Fig. 3, the calculations carried out by the TDHF equations illustrate very nicely the expected the mean-drift paths in the collision of $^{48}\text{Ca} + ^{238}\text{U}$ system with the several impact parameters. Since the charge asymmetries of ^{48}Ca and ^{238}U are very close to the charge asymmetry of the composite system, a rapid equilibration of the charge asymmetry is not very visible in this system. We observe that the di-nuclear system drifts towards symmetry during long contact time, but separates before reaching to the symmetry. Following this observation and borrowing an idea from references [68,72], for each impact parameter, we parameterize the N_1 and Z_1 dependence of the potential energy surface of the di-nuclear system in terms of two parabolic forms,

$$U(N_1, Z_1) = \frac{1}{2}a(\tilde{z}\cos\phi - \tilde{n}\sin\phi)^2 + \frac{1}{2}b(z\sin\phi + n\cos\phi)^2. \quad (38)$$

Here, the first term describes a strong driving force perpendicular to the mean-drift path. The quantity $\tilde{z}\cos\phi - \tilde{n}\sin\phi$ denotes the perpendicular distance of a di-nuclear state with N_1, Z_1 from the mean-drift with $\tilde{z} = Z_f - Z_1$ and $\tilde{n} = N_f - N_1$. The angle between the mean-drift path and the N axis is indicated by ϕ . Here N_f and Z_f are the mean values of neutron and proton numbers of the light fragment just after the separation. The second parabola describes a relative weak driving force toward symmetry along the stability valley. The quantity $z\sin\phi + n\cos\phi$ indicates the distance of the di-nuclear state with N_1, Z_1 state along the mean-drift path from the symmetry with $z = Z_0 - Z_1$ and $n = N_0 - N_1$. The quantities N_0 and Z_0 denotes the equilibrium values of the neutron and proton numbers, which are determined by the average values of the neutron and proton numbers of the projectile and target, $N_0 = (N_P + N_T)/2$ and $Z_0 = (Z_P + Z_T)/2$. The parameters of the driving potential depend on the impact parameter. We

can determine the values of Z_f and N_f from the mean-drift path for each impact parameter. Also, we observe from Fig. 3 that the slope of the mean-drift paths is nearly the same for different impact parameters. Therefore the angle $\phi \approx 32^\circ$ is approximately the same for different impact parameters. Following from the fluctuation-dissipation theorem, it is possible to relate the proton and neutron drift coefficients to the diffusion coefficients and the associated driving forces, in terms of the Einstein relations as follows [71,72],

$$v_n = -\frac{D_{NN}}{T} \frac{\partial U}{\partial N_1} = D_{NN} [-\alpha \sin \phi (\tilde{z} \cos \phi - \tilde{n} \sin \phi) + \beta \cos \phi (z \sin \phi + n \cos \phi)], \quad (39)$$

and

$$v_z = -\frac{D_{ZZ}}{T} \frac{\partial U}{\partial Z_1} = D_{ZZ} [+ \alpha \cos \phi (\tilde{z} \cos \phi - \tilde{n} \sin \phi) + \beta \sin \phi (z \sin \phi + n \cos \phi)]. \quad (40)$$

Here the temperature T factor is absorbed into curvature co-

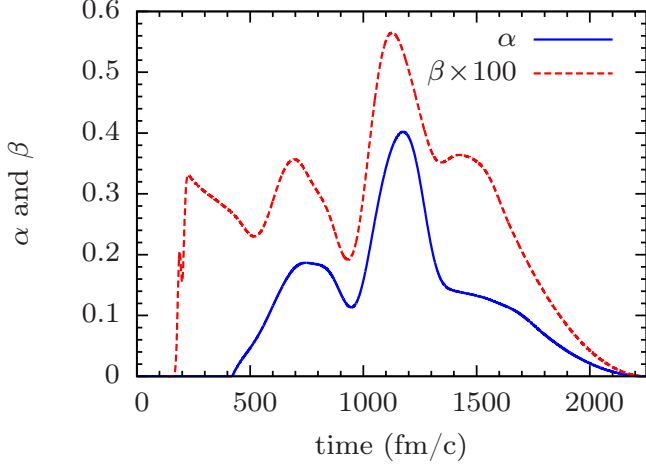


FIG. 5. (color online) Curvature parameters α and β as a function of time in the $^{48}\text{Ca} + ^{238}\text{U}$ collisions in the tip geometry of the uranium at $E_{\text{c.m.}} = 193$ MeV and impact parameter $b = 2.8$ fm.

efficients, $\alpha = a/T$ and $\beta = b/T$, consequently temperature does not appear as a parameter in the description. We can determine α and β by matching the mean values of neutron and proton drift coefficients obtained from the TDHF solutions. In this manner, microscopic description of the collision geometry and details of the dynamical effects are incorporated into the drift coefficients. As an example, Fig. 5 illustrates the curvature parameters α and β as a function of time in the $^{48}\text{Ca} + ^{238}\text{U}$ collisions in the tip geometry of the uranium at $E_{\text{c.m.}} = 193$ MeV and impact parameter $b = 2.8$ fm.

The curvature parameters are positive as expected from the potential energy surface, but as a result of the quantal effects arising mainly from the shell structure, they exhibit fluctuations as a function of time. Time dependence can also be viewed as a dependence on the relative distance between ions. In differential equations (17-19) for co-variances, we need the

derivatives of drift coefficients with respect to proton and neutron numbers of projectile-like fragments. As a great advantage of this approach, we can easily calculate these derivatives from drift coefficients to yield,

$$\frac{\partial v_n}{\partial N_1} = -D_{NN} (\alpha \sin^2 \phi + \beta \cos^2 \phi), \quad (41)$$

$$\frac{\partial v_z}{\partial Z_1} = -D_{ZZ} (\alpha \cos^2 \phi + \beta \sin^2 \phi), \quad (42)$$

$$\frac{\partial v_n}{\partial Z_1} = -D_{NN} (\beta - \alpha) \sin \phi \cos \phi, \quad (43)$$

$$\frac{\partial v_z}{\partial N_1} = -D_{ZZ} (\beta - \alpha) \sin \phi \cos \phi. \quad (44)$$

The curvature parameter α perpendicular to the beta stability valley is much larger than the curvature parameter β along the stability valley. Consequently, β does not have an appreciable effect on the derivatives of the drift coefficients. We determine the co-variances $\sigma_{NN}^2(t)$, $\sigma_{ZZ}^2(t)$ and $\sigma_{NZ}^2(t)$ for each impact parameter by solving the coupled differential equations (17-19) with the initial conditions $\sigma_{NN}^2(0) = 0$, $\sigma_{ZZ}^2(0) = 0$ and $\sigma_{NZ}^2(0) = 0$. As an example Fig. 6 shows the co-variances as a function of time in the $^{48}\text{Ca} + ^{238}\text{U}$ collisions in the tip geometry of the uranium at $E_{\text{c.m.}} = 193$ MeV and impact parameter $b = 2.8$ fm. The variance of the fragment mass distribution $\sigma_{AA}^2(t)$ is determined as

$$\sigma_{AA}^2(t) = \sigma_{NN}^2(t) + \sigma_{ZZ}^2(t) + 2\sigma_{NZ}^2(t). \quad (45)$$

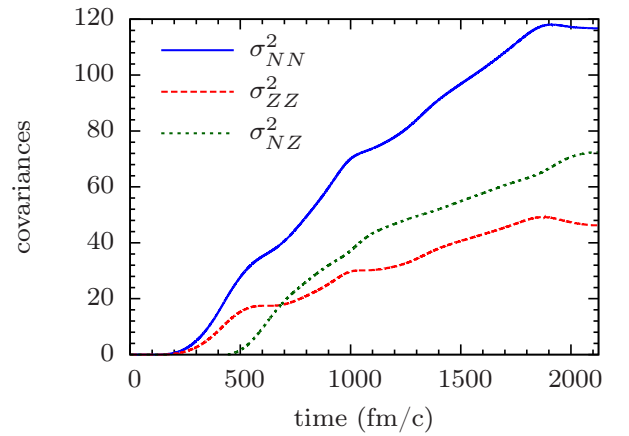


FIG. 6. (color online) Co-variances as a function of time in the $^{48}\text{Ca} + ^{238}\text{U}$ collisions in the tip geometry of the uranium at $E_{\text{c.m.}} = 193$ MeV and impact parameter $b = 2.8$ fm.

IV. FRAGMENT MASS DISTRIBUTION IN $^{48}\text{Ca} + ^{238}\text{U}$ COLLISIONS

In the computation of the production cross-sections of fragments as a function of the charge and mass of the fragments, we need to include all relevant impact parameters (or the initial orbital angular momenta) and as well as an average of fragment probabilities over all possible orientations of the target nucleus ^{238}U . In the experimental investigations of Kozulin *et al.* [1] for the $^{48}\text{Ca} + ^{238}\text{U}$ system, the detectors are placed between the angles $+64^\circ$ and -64° with $\pm 10^\circ$ acceptance range in the laboratory frame. We consider the data collected at $E_{\text{c.m.}} = 193$ MeV which corresponds to $E_{\text{lab}} = 232$ MeV. In order to determine the dominant geometry of the target nucleus, we consider three perpendicular configurations of the target which includes “tip”, “side-p” and “side-s” orientations. In the “tip” orientation the symmetry axis of uranium is parallel to the beam direction. In the “side-p” and “side-s” orientations the symmetry axis of uranium is perpendicular to the beam direction as well as parallel and perpendicular to the reaction plane, respectively. For a given impact parameter, the laboratory scattering angles θ_1^{lab} , θ_2^{lab} of the fragments are related to the center of mass scattering angle $\theta_{\text{c.m.}}$ according to,

$$\tan \theta_1^{\text{lab}} = \frac{\sin \theta_{\text{c.m.}}}{\sqrt{\frac{A_1^i A_1^f E_{\text{c.m.}}}{A_2^i A_2^f TKE} + \cos \theta_{\text{c.m.}}}}, \quad (46)$$

and

$$\tan \theta_2^{\text{lab}} = \frac{\sin \theta_{\text{c.m.}}}{\sqrt{\frac{A_1^i A_2^f E_{\text{c.m.}}}{A_1^f A_2^i TKE} - \cos \theta_{\text{c.m.}}}}. \quad (47)$$

Here, A_1^i , A_2^i and A_1^f , A_2^f denote the initial and final mass numbers of the fragments, and TKE is the total kinetic energy of the fragments after the collision. We calculate the scattering angles at $E_{\text{c.m.}} = 193$ MeV with different impact parameters for different geometries employing the TDHF description. We find that at this c.m. energy, “side-p” and “side-s” configurations do not lead to the experimental scattering angle range with any impact parameter. Therefore, we assume that the dominant contribution to the experimental range arise from the “tip” configuration of the uranium nucleus. This assumption is supported by the recent investigation of [13]. We find that the collisions in the “tip” orientation with the initial orbital angular momenta interval $40\hbar \leq \ell \leq 62\hbar$ reaches to the experimental acceptance range. In order to save computation time, we introduce a coarse grained approximation by carrying out the calculations only for even values of the orbital angular momentum and taking a range $\Delta\ell = 2\hbar$ as the angular momentum interval. As seen from tables I and II, the observable quantities are monotonically changing with the angular momentum, which indicates that this is a reasonable approximation. Tables I and II present the results of the TDHF calculations in the “tip” orientation. Table I shows the initial orbital angular momentum ℓ_i , the corresponding impact parameter b_i , the final orbital angular momentum ℓ_f , the final average total

kinetic energy TKE , the average total excitation energy E^* , the center of mass scattering angle $\theta_{\text{c.m.}}$, and scattering angles θ_1^{lab} , θ_2^{lab} of the fragments in the lab frame, respectively. We calculate the mean excitation energies employing the expression, $E^* = E_{\text{c.m.}} + Q - TKE$, where Q represents the Q -value of the channel. Table II shows the mass and charge numbers A_1^f , A_2^f , Z_1^f , Z_2^f of the final fragments, co-variances σ_{NN}^2 , σ_{ZZ}^2 , σ_{NZ}^2 for each orbital angular momentum. We evaluate the

TABLE I. The impact parameter b_i , the final orbital angular momentum ℓ_f , the final average total kinetic energy TKE , the average total excitation energy E^* and scattering angles corresponding to the initial orbital angular momentum ℓ_i .

$\ell_i (\hbar)$	$b_i (\text{fm})$	$\ell_f (\hbar)$	$TKE (\text{MeV})$	$E^* (\text{MeV})$	$\theta_{\text{c.m.}}$	θ_1^{lab}	θ_2^{lab}
40	2.10	36.3	200.6	76.0	100.5	73.6	47.5
42	2.20	35.8	198.4	78.2	100.2	73.2	47.6
44	2.31	38.3	193.5	82.3	96.0	69.4	49.6
46	2.41	36.8	194.2	81.6	92.3	66.3	52.2
48	2.51	38.1	195.3	80.5	90.5	65.0	53.2
50	2.62	40.5	193.0	78.7	87.5	62.4	54.9
52	2.72	45.0	195.4	80.4	83.1	59.0	58.3
54	2.82	46.8	199.2	76.6	80.8	57.3	60.2
56	2.93	46.1	198.2	77.6	76.8	54.2	62.7
58	3.03	47.6	190.6	81.1	73.5	51.4	64.1
60	3.14	50.5	184.1	80.9	78.7	55.1	59.1
62	3.24	49.8	180.4	76.8	88.1	62.4	52.4

TABLE II. The mass and charge numbers A_1^f , A_2^f , Z_1^f , Z_2^f of the final fragments, co-variances σ_{NN}^2 , σ_{ZZ}^2 , σ_{NZ}^2 for each initial orbital angular momentum ℓ_i .

$\ell_i (\hbar)$	A_1^f	Z_1^f	A_2^f	Z_2^f	σ_{NN}^2	σ_{ZZ}^2	σ_{NZ}^2
40	78.4	31.5	207.6	80.5	159.3	67.4	75.2
42	77.6	31.3	208.4	80.7	144.8	58.4	77.2
44	76.7	31.0	209.3	81.0	147.4	62.3	63.0
46	77.3	31.1	208.7	80.9	139.6	57.7	75.0
48	76.6	30.8	209.4	81.2	149.1	66.4	59.7
50	76.2	30.6	209.8	81.4	135.9	54.3	71.7
52	77.4	31.1	208.6	80.9	154.3	65.5	64.5
54	77.7	31.3	208.3	80.7	116.8	46.3	72.4
56	76.8	31.0	209.2	81.0	116.0	45.7	72.1
58	76.3	30.7	209.7	81.3	112.4	44.1	70.0
60	73.5	29.8	212.5	82.2	100.5	40.0	60.9
62	71.7	29.0	214.3	83.0	76.8	30.1	47.2

mass distributions of the primary fragments as the initial angular momentum weighted average of the Gaussian functions given in Eq. (23),

$$P(A) = \frac{\eta}{\sum_{\ell} (2\ell + 1)} \sum_{\ell} (2\ell + 1) [P_{\ell}(A - A_{1,\ell}) + P_{\ell}(A - A_{2,\ell})], \quad (48)$$

where the first and second Gaussians describe the mass distribution of the projectile-like and the target-like fragments with the same dispersions $\sigma_{AA}(\ell)$ and the mean values $A_{1,\ell}$,

$A_{2,\ell}$, respectively. In this expression η is a normalization constant and the summations run over angular momentum range shown in Table I, $40 \leq \ell \leq 62$, which approximately corresponds to the data collected in the experiment reported by Kozulin *et al.* [1]. We determine the normalization constant η by matching the peak value of the experimental yield at $A = 210$ to give a value $\eta = 214$ for the normalization. The normalization constant η determines the integrated yield between the peak values $76 \leq A \leq 210$ of the calculated distribution function. In order to make a comparison with the data, we calculate the area under the data curve within the same interval $76 \leq A \leq 210$ which gives a value of 280 for the experimental yield. This experimental yield includes the totally relaxed events within the interval $76 \leq A \leq 210$ and also includes the fusion-fission events. Since the deep inelastic events are excluded, there are no data points outside the range $70 \leq A \leq 220$ in Fig. 7. On the other hand, the quantal diffusion calculations presented here includes the totally relaxed as well as the deep-inelastic events, but not the fusion-fission events. Comparing the integrated yield with the experimen-

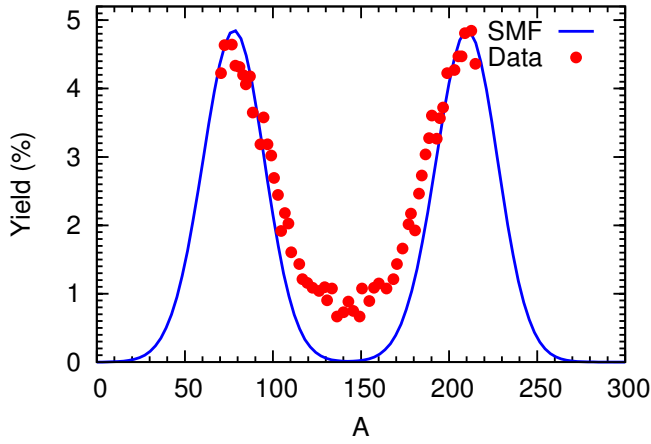


FIG. 7. (color online) Primary fragment yield in the $^{48}\text{Ca} + ^{238}\text{U}$ collisions at $E_{\text{c.m.}} = 193$ MeV and comparison with data. The solid line is the result of Eq. (48).

tal yield in the interval $76 \leq A \leq 210$, the calculation predicts an integrated yield of $280 - 214 = 66$, which is about 23% of the total yield, for the fusion-fission events. It is also possible to calculate the cross sections for the primary fragments as a function of neutron and proton numbers by employing Eq. (22) in discrete form,

$$\sigma(N, Z) = \frac{\pi \hbar^2}{\mu E_{\text{c.m.}}} \sum_{\ell} (2\ell + 1) P_{\ell}(N, Z). \quad (49)$$

Since the sum runs over even ℓ values, there is no factor of 2 in the denominator. Here, we express the cross-section in terms of the initial orbital angular momenta, rather than the impact parameters. The summation is over the initial orbital angular momenta listed in Table I and μ is the reduced mass of the projectile and target nuclei. Figure 8 shows the contour plots of the calculated cross-section for producing primary target-like fragments, in (N, Z) plane in units of millibarn, in the

$^{48}\text{Ca} + ^{238}\text{U}$ collisions with the c.m. energy $E_{\text{c.m.}} = 193$ MeV. Experimental data is not available in [1] to compare with the calculated cross-sections.

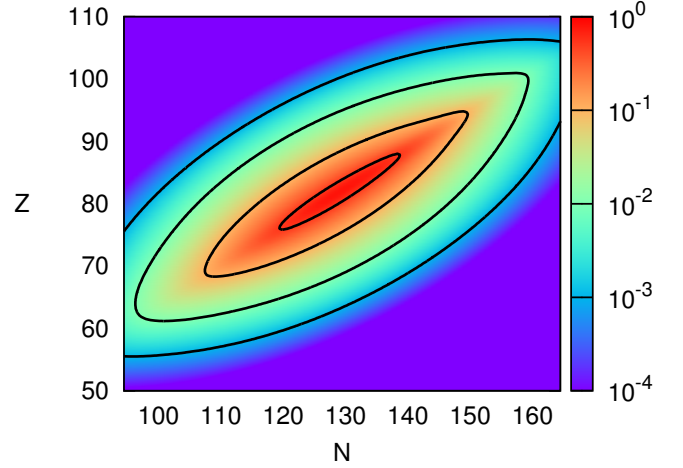


FIG. 8. (color online) Calculated primary fragment production cross-section for the $^{48}\text{Ca} + ^{238}\text{U}$ collisions at $E_{\text{c.m.}} = 193$ MeV in (N, Z) plane in units of millibarn.

V. CONCLUSIONS

We present a quantal diffusion description for multi-nucleon exchange mechanism in dissipative heavy-ion collisions in the di-nuclear regime. The diffusion description is deduced by employing the relevant macroscopic variables in the SMF approach. In the SMF approach the collision dynamics is described by an ensemble of mean-field events. The initial conditions for the events are specified by the quantal and thermal fluctuations in the initial state. In the di-nuclear regime of the collision, reaction predominantly occurs by nucleon exchange through the window between the projectile and target nuclei. It is possible to define the neutron and the proton numbers of projectile-like and target-like fragments, relative momentum and other macroscopic variables in each event with the help of the window dynamics by integrating the relevant quantities in both side of the window over the TDHF density. The SMF approach gives rise to Langevin description for the evolution of macroscopic variables. The Langevin description is equivalent to the Fokker-Plank transport equation for distribution function of the macroscopic variables. The transport approach is characterized by diffusion and drift coefficients for macroscopic variable. In this study, we consider charge and mass asymmetry as the macroscopic variables and drive analytical quantal expressions for the associated transport coefficients. These transport coefficient are determined entirely in terms of the mean-field properties provided the solutions of the TDHF equations. The description of mean values and the fluctuation of the macroscopic variables are determined by the set of occupied single-particle wave functions of the TDHF approach. This important result is a reflection of the fluctuation-dissipation relation of the non-equilibrium quan-

tum statistical mechanics. Quantal diffusion description includes the full geometry of the collision dynamics and does not involve any adjustable parameter other than the Skyrme parameters of the TDHF.

As a first application, we applied the quantal diffusion approach to study multi-nucleon transfer in the $^{48}\text{Ca} + ^{238}\text{U}$ collisions at $E_{\text{c.m.}} = 193$ MeV. During the long interaction times, of the order of 2000 fm/c, the di-nuclear system drift toward symmetry by transferring nearly 20 neutrons and 10 protons to the projectile. The large drift is accompanied with a broad charge and mass distribution with a mass dispersion in the order of 18 atomic mass unit. We have calculated the cross-sections for produced fragments as a function of neutron and proton number, as well as the mass distributions of the primary fragments. In this work, we don't carry out the de-excitation calculations. However, because of the relatively low excitation energies of the fragments, we expect de-excitation mechanism to not to alter the primary fragment distributions appreciably. We analyze the data for the $^{48}\text{Ca} + ^{238}\text{U}$ collisions at $E_{\text{c.m.}} = 193$ MeV published by Kozulin *et al.* [1]. The calculations provide a good description of the measured fragment mass distribution.

ACKNOWLEDGMENTS

S.A. gratefully acknowledges the IPN-Orsay and the Middle East Technical University for warm hospitality extended to him during his visits. S.A. also gratefully acknowledges useful discussions with D. Lacroix, and very much thankful to F. Ayik for continuous support and encouragement. This work is supported in part by US DOE Grant Nos. DE-SC0015513 and DE-SC0013847, and in part by TUBITAK Grant No. 117F109.

Appendix A: Window dynamics

We can determine the orientation of symmetry axis of the di-nuclear system with the help of the mass quadrupole moment of the di-nuclear system. In the center of mass system, the element of the quadrupole matrix is given by

$$Q_{ij} = 3\sigma_{ij} - \left(\sum_k \sigma_{kk} \right) \delta_{ij}, \quad (\text{A1})$$

here i, j, k indices take values 1, 2, 3 and $x_1, x_2, x_3 \rightarrow x, y, z$. In this expression the elements of the sigma matrix are defined in terms of the position co-variances as,

$$\begin{aligned} \sigma_{ij}(t) &= \sum_h \langle \phi_h(t) | x_i x_j | \phi_h(t) \rangle \\ &- \sum_{h,h'} \langle \phi_h(t) | x_i | \phi_h(t) \rangle \langle \phi_{h'}(t) | x_j | \phi_{h'}(t) \rangle. \end{aligned} \quad (\text{A2})$$

We can determine the direction of the symmetry axis, with the elements of the quadrupole matrix in reaction plane which is defined by $z = 0$. In this case, we just need to diagonalize the

2×2 reduced quadrupole matrix on the reaction plane with elements $Q_{xx}, Q_{xy}, Q_{yx}, Q_{yy}$. The eigenvectors \vec{E}_+ and \vec{E}_- of the quadrupole matrix specify the principal axes of the di-nuclear mass distribution on the reaction plane. These eigenvectors have the following form,

$$\vec{E}_{\pm} = \begin{pmatrix} Q_{\pm} \\ 1 \end{pmatrix}, \quad (\text{A3})$$

with components given by

$$Q_{\pm} = \frac{Q_{xx} - Q_{yy} \pm \sqrt{(Q_{xx} - Q_{yy})^2 + 4Q_{xy}^2}}{2Q_{xy}}. \quad (\text{A4})$$

The eigenvalues Γ_{\pm} corresponding to Q_{\pm} are given by,

$$\Gamma_{\pm} = \frac{Q_{xx} + Q_{yy} \pm \sqrt{(Q_{xx} - Q_{yy})^2 + 4Q_{xy}^2}}{2}. \quad (\text{A5})$$

The beam direction as taken in the x direction in the fixed coordinate system (x, y) . The eigenvectors of the quadrupole matrix define a rotated orthogonal system in the reaction plane with axes pointing along \vec{E}_+ and \vec{E}_- directions. We note that the eigenvalue Γ_+ is larger than the eigenvalue Γ_- . The eigenvector \vec{E}_+ associated with the large eigenvalue Γ_+ specifies the direction of the symmetry axis of the di-nuclear system. The angle θ between the positive direction of the x -axis and the direction of $\vec{E}_+ = (Q_+, 1)$ is determined by

$$\tan \theta = \frac{1}{Q_+} = \frac{2Q_{xy}}{Q_{xx} - Q_{yy} + \sqrt{(Q_{xx} - Q_{yy})^2 + 4Q_{xy}^2}} \quad (\text{A6})$$

Using the trigonometric identity,

$$\tan \theta = \frac{\tan 2\theta}{1 + \sqrt{1 + \tan^2 2\theta}}, \quad -\frac{\pi}{2} < \theta < +\frac{\pi}{2} \quad (\text{A7})$$

and

$$\tan \theta = \frac{\tan 2\theta}{1 - \sqrt{1 + \tan^2 2\theta}}, \quad +\frac{\pi}{2} < \theta < +\frac{3\pi}{2} \quad (\text{A8})$$

we can express the angle θ symmetry axis in terms of the elements of the elements of the quadrupole or the elements of sigma matrix as,

$$\tan 2\theta = \frac{2Q_{xy}}{Q_{xx} - Q_{yy}} = \frac{2\sigma_{xy}}{\sigma_{xx} - \sigma_{yy}} \quad (\text{A9})$$

which applies to the entire range specified in (A7) and (A8).

Appendix B: Analysis of the closure relation

We re-write Eq. (32) as,

$$\begin{aligned} \sum_{a \in P, h \in T} A_{ah}^{\alpha}(t) A_{ah}^{*\alpha}(t') &= \sum_{h \in T} \int d^3 R d^3 r \delta(\vec{r} + \vec{u}_h \tau) \\ &\times W_h^{\alpha}(\vec{r}_1, t) W_h^{*\alpha}(\vec{r}_2, t'), \end{aligned} \quad (\text{B1})$$

in which we introduce the coordinate transformation,

$$\vec{R} = (\vec{r}_1 + \vec{r}_2)/2, \quad \vec{r} = \vec{r}_1 - \vec{r}_2, \quad (\text{B2})$$

and its reverse as

$$\vec{r}_1 = \vec{R} + \vec{r}/2, \quad \vec{r}_2 = \vec{R} - \vec{r}/2. \quad (\text{B3})$$

For clearness, we present quantities $W_h^\alpha(\vec{r}_1, t)$ and $W_h^{*\alpha}(\vec{r}_2, t')$ here again,

$$W_h^\alpha(\vec{r}_1, t) = \frac{\hbar}{m} g(x'_1) \times \left(\hat{e} \cdot \vec{\nabla}_1 \Phi_h^\alpha(\vec{r}_1, t) - \frac{x'_1}{2\kappa^2} \Phi_h^\alpha(\vec{r}_1, t) \right), \quad (\text{B4})$$

and

$$W_h^{*\alpha}(\vec{r}_2, t') = \frac{\hbar}{m} g(x'_2) \times \left(\hat{e} \cdot \vec{\nabla}_2 \Phi_h^{*\alpha}(\vec{r}_2, t') - \frac{x'_2}{2\kappa^2} \Phi_h^{*\alpha}(\vec{r}_2, t') \right). \quad (\text{B5})$$

Because of the delta function in the integrand of Eq. (B1), we make the substitution $\vec{r} = -\vec{u}_h^\alpha(\vec{R}, T)\tau$ in the wave functions and introduce the backward diabatic shift to obtain,

$$\Phi_h^\alpha(\vec{R} + \vec{r}/2, t) = \Phi_h^\alpha(\vec{R} - \vec{u}_h^\alpha\tau/2, t) \approx \Phi_h^\alpha(\vec{R}, T), \quad (\text{B6})$$

and

$$\Phi_h^\alpha(\vec{R} - \vec{r}/2, t') = \Phi_h^\alpha(\vec{R} + \vec{u}_h^\alpha\tau/2, t') \approx \Phi_h^\alpha(\vec{R}, T). \quad (\text{B7})$$

The local flow velocity of the wave function $\Phi_h^\alpha(\vec{R}, T)$ is calculated in the standard manner,

$$\vec{u}_h^\alpha(\vec{R}, T) = \frac{\hbar}{m} \frac{1}{|\Phi_h^\alpha(\vec{R}, T)|^2} \text{Im} \left(\Phi_h^{*\alpha}(\vec{R}, T) \nabla \Phi_h^\alpha(\vec{R}, T) \right), \quad (\text{B8})$$

with $T = (t + t')/2 = t - \tau/2$. We write the product of Gaussian factors as

$$g(x'_1)g(x'_2) = \tilde{g}(X')\tilde{G}(x'), \quad (\text{B9})$$

with

$$\tilde{g}(X') = \frac{1}{\sqrt{\pi\kappa}} \exp \left[-\left(\frac{X'}{\kappa} \right)^2 \right], \quad (\text{B10})$$

and

$$\tilde{G}(x') = \frac{1}{\sqrt{4\pi\kappa}} \exp \left[-\left(\frac{x'}{2\kappa} \right)^2 \right]. \quad (\text{B11})$$

In these Gaussians following the transformations below Eq. (4), the coordinates in the rotating frame are expressed in terms of the coordinates in the fixed frame as, $X' = (X -$

$x_0) \cos \theta + (Y - y_0) \sin \theta$ and $x' = x \cos \theta + y \sin \theta$. Carrying out the product of the factors and making the substitution $\vec{r} = -\vec{u}_h^\alpha(\vec{R}, T)\tau$, Eq. (B1) becomes,

$$\sum_{a \in P, h \in T} A_{ah}^\alpha(t) A_{ah}^{*\alpha}(t') = \left(\frac{\hbar}{m} \right)^2 \sum_{h \in T} \int d^3R \tilde{g}(X') \frac{G_T^h(\tau)}{|u_\perp^h(\vec{R}, T)|} \times \left[|\hat{e} \cdot \vec{\nabla} \Phi_h^\alpha(\vec{R}, T)|^2 + \frac{X'^2 - (u_\perp^h\tau/2)^2}{4\kappa^4} |\Phi_h^\alpha(\vec{R}, T)|^2 - \frac{X'}{2\kappa^2} \hat{e} \cdot \vec{\nabla} (|\Phi_h^\alpha(\vec{R}, T)|^2) \right]. \quad (\text{B12})$$

Here, $u_\perp^h(\vec{R}, T)$ represents the component of the nucleon (proton or neutron) flow velocity perpendicular to the window $u_\perp^h(\vec{R}, T) = \hat{e} \cdot \vec{u}_T^h(\vec{R}, T)$ and $G_h(\tau)$ indicates the memory kernel,

$$G_T^h(\tau) = \frac{1}{\sqrt{4\pi}} \frac{1}{\tau_T^h} \exp[-(\tau/2\tau_T^h)^2], \quad (\text{B13})$$

with the memory time $\tau_T^h = \kappa/|u_\perp^h|$. In this expression $\tilde{g}(X')$ is sharp as Gaussian smoothing function centered on the window with a dispersion $\kappa = 0.5$ fm due to the fact that $\tilde{g}(X')$ is centered at $X' = 0$, the third term in Eq. (B12) is nearly zero. In the second term, after carrying out an average over the memory, the factor in the middle becomes,

$$X'^2 - (u_\perp^h\tau/2)^2 \rightarrow X'^2 - (\kappa/2)^2. \quad (\text{B14})$$

Since Gaussian $\tilde{g}(X')$ is sharply peaked around $X' = 0$ with a variance $(\kappa/2)^2$, the second terms in Eq. (B12) is expected to be very small, as well. Neglecting the second and third terms, Eq. (B1) becomes,

$$\sum_{a \in P, h \in T} A_{ah}^\alpha(t) A_{ah}^{*\alpha}(t') = \left(\frac{\hbar}{m} \right)^2 \sum_{h \in T} \int d^3R \tilde{g}(X') \frac{G_T^h(\tau)}{|u_\perp^h(\vec{R}, T)|} \times |\hat{e} \cdot \vec{\nabla} \Phi_h^\alpha(\vec{R}, T)|^2. \quad (\text{B15})$$

In the continuation, we express the wave functions in terms of its magnitude and its phase as [73],

$$\Phi_h^\alpha(\vec{R}, T) = |\Phi_h^\alpha(\vec{R}, T)| \exp \left(iQ_h^\alpha(\vec{R}, T) \right). \quad (\text{B16})$$

The phase factor $Q_h^\alpha(\vec{R}, T)$ behaves as the velocity potential of the flow velocity of the wave. Using the definition given by Eq. (B8), we observe that the flow velocity is given by $\vec{u}_h^\alpha(\vec{R}, T) = (\hbar/m) \vec{\nabla} Q_h^\alpha(\vec{R}, T)$. In the vicinity of the window, in the perpendicular direction, the phase factors varies faster than the magnitude of the wave functions. Neglecting the variation of the magnitude $|\Phi_h^\alpha(\vec{R}, T)|$ in the vicinity of the window, we can express the gradient of the wave function in Eq. (B12) as,

$$\hat{e} \cdot \vec{\nabla} \Phi_h^\alpha(\vec{R}, T) \approx iQ_h^\alpha(\vec{R}, T) \left(\hat{e} \cdot \vec{\nabla} Q_h^\alpha(\vec{R}, T) \right), \quad (\text{B17})$$

where the quantity inside the parenthesis is the component of the nucleon flow velocity perpendicular to the window. As a

result, Eq. (B1) becomes,

$$\sum_{a \in P, h \in T} A_{ah}^\alpha(t) A_{ah}^{*\alpha}(t') = \int d^3 R \tilde{g}(X') \vec{j}_{\perp, \alpha}^T(\vec{R}, t - \tau/2). \quad (\text{B18})$$

Here, $\vec{j}_{\perp, \alpha}^T(\vec{R}, t - \tau/2)$ represents the magnitude of the current densities perpendicular to the window due to each wave functions originating from target and each term multiplied by the memory kernel,

$$\vec{j}_{\perp, \alpha}^T(\vec{R}, T) = \frac{\hbar}{m} \sum_{h \in T} G_T^h(\tau) \times \left| \text{Im} \left[\Phi_h^*(\vec{R}, T) \left(\hat{e} \cdot \vec{\nabla} \Phi_h(\vec{R}, T) \right) \right] \right|. \quad (\text{B19})$$

In Eq. (33) we introduce a further approximation by replacing the individual memory kernels $G_T^h(\tau)$ by its average value taken over the hole states,

$$G_T(\tau) = \frac{1}{\sqrt{4\pi\tau_T}} \exp[-(\tau/2\tau_T)^2], \quad (\text{B20})$$

with the memory time determined by the average speed u_T by $\tau_T = \kappa/|u_T(t)|$. The average value $u_T^h(t)$ of the flow speed for each hole state across the window is calculated as $u_T^h(t) = \int d^3 R \tilde{g}(X') \hat{e} \cdot \vec{j}_T^h(\vec{R}, t) / \int d^3 R \tilde{g}(X') \rho_T^h(\vec{R}, t)$ where $\vec{j}_T^h(\vec{R}, t)$ and $\rho_T^h(\vec{R}, t)$ denote the current density and density of hole state originating from target, respectively. The average $|u_T(t)|$ is then calculated by taking the mean value of all the flow speeds $|u_T^h(t)|$ of the hole states. It is possible to calculate the average speed from $u_T(t) = \int d^3 R \tilde{g}(X') \hat{e} \cdot \vec{j}_T(\vec{R}, t) / \int d^3 R \tilde{g}(X') \rho_T(\vec{R}, t)$, where $\rho_T(\vec{R}, t)$ and $\vec{j}_T(\vec{R}, t)$ are the total density and the total current density of the states originating from the target. We expect both average speeds have nearly the same magnitude.

-
- [1] E. M. Kozulin, G. N. Knyazheva, I. M. Itkis, N. I. Kozulina, T. A. Loktev, K. V. Novikov, and I. Harca, “Shell effects in fission, quasifission and multinucleon transfer reaction,” *J. Phys. Conf. Ser.* **515**, 012010 (2014).
- [2] E. M. Kozulin, G. N. Knyazheva, S. N. Dmitriev, I. M. Itkis, M. G. Itkis, T. A. Loktev, K. V. Novikov, A. N. Baranov, W. H. Trzaska, E. Vardaci, S. Heinz, O. Beliuskina, and S. V. Khlebnikov, “Shell effects in damped collisions of ^{88}Sr with ^{176}Yb at the Coulomb barrier energy,” *Phys. Rev. C* **89**, 014614 (2014).
- [3] J. Töke, R. Bock, G. X. Dai, A. Gobbi, S. Gralla, K. D. Hildenbrand, J. Kuzminski, W. F. J. Müller, A. Olmi, H. Stelzer, B. B. Back, and S. Bjørnholm, “Quasi-fission: The mass-drift mode in heavy-ion reactions,” *Nucl. Phys. A* **440**, 327–365 (1985).
- [4] W. Q. Shen, J. Albinski, A. Gobbi, S. Gralla, K. D. Hildenbrand, N. Herrmann, J. Kuzminski, W. F. J. Müller, H. Stelzer, J. Töke, B. B. Back, S. Bjørnholm, and S. P. Sørensen, “Fission and quasifission in U-induced reactions,” *Phys. Rev. C* **36**, 115–142 (1987).
- [5] D. J. Hinde, D. Hilscher, H. Rossner, B. Gebauer, M. Lehmann, and M. Wilpert, “Neutron emission as a probe of fusion-fission and quasi-fission dynamics,” *Phys. Rev. C* **45**, 1229–1259 (1992).
- [6] D. J. Hinde, M. Dasgupta, J. R. Leigh, J. P. Lestone, J. C. Mein, C. R. Morton, J. O. Newton, and H. Timmers, “Fusion-Fission versus Quasifission: Effect of Nuclear Orientation,” *Phys. Rev. Lett.* **74**, 1295–1298 (1995).
- [7] D. J. Hinde, M. Dasgupta, J. R. Leigh, J. C. Mein, C. R. Morton, J. O. Newton, and H. Timmers, “Conclusive evidence for the influence of nuclear orientation on quasifission,” *Phys. Rev. C* **53**, 1290–1300 (1996).
- [8] M. G. Itkis, J. Äystö, S. Beghini, A. A. Bogachev, L. Corradi, O. Dorvaux, A. Gadea, G. Giardina, F. Hanappe, I. M. Itkis, M. Jandel, J. Kliman, S. V. Khlebnikov, G. N. Kniajeva, N. A. Kondratiev, E. M. Kozulin, L. Krupa, A. Latina, T. Materna, G. Montagnoli, Yu. Ts. Oganessian, I. V. Pokrovsky, E. V. Prokhorova, N. Rowley, V. A. Rubchenya, A. Ya. Rusanov, R. N. Sagaidak, F. Scarlassara, A. M. Stefanini, L. Stuttge,
- S. Szilner, M. Trotta, W. H. Trzaska, D. N. Vakhtin, A. M. Vinodkumar, V. M. Voskressenski, and V. I. Zagrebaev, “Shell effects in fission and quasi-fission of heavy and superheavy nuclei,” *Nucl. Phys. A* **734**, 136–147 (2004).
- [9] G. N. Knyazheva, E. M. Kozulin, R. N. Sagaidak, A. Yu. Chizhov, M. G. Itkis, N. A. Kondratiev, V. M. Voskressenski, A. M. Stefanini, B. R. Behera, L. Corradi, E. Fioretto, A. Gadea, A. Latina, S. Szilner, M. Trotta, S. Beghini, G. Montagnoli, F. Scarlassara, F. Haas, N. Rowley, P. R. S. Gomes, and A. Szanto de Toledo, “Quasifission processes in $^{40,48}\text{Ca} + ^{144,154}\text{Sm}$ reactions,” *Phys. Rev. C* **75**, 064602 (2007).
- [10] D. J. Hinde, R. G. Thomas, R. du Rietz, A. Diaz-Torres, M. Dasgupta, M. L. Brown, M. Evers, L. R. Gasques, R. Rafiei, and M. D. Rodriguez, “Disentangling Effects of Nuclear Structure in Heavy Element Formation,” *Phys. Rev. Lett.* **100**, 202701 (2008).
- [11] K. Nishio, H. Ikezoe, S. Mitsuoka, I. Nishinaka, Y. Nagame, Y. Watanabe, T. Ohtsuki, K. Hirose, and S. Hofmann, “Effects of nuclear orientation on the mass distribution of fission fragments in the reaction of $^{36}\text{S} + ^{238}\text{U}$,” *Phys. Rev. C* **77**, 064607 (2008).
- [12] R. du Rietz, D. J. Hinde, M. Dasgupta, R. G. Thomas, L. R. Gasques, M. Evers, N. Lobanov, and A. Wakhle, “Predominant Time Scales in Fission Processes in Reactions of S, Ti and Ni with W: Zeptosecond versus Attosecond,” *Phys. Rev. Lett.* **106**, 052701 (2011).
- [13] I. M. Itkis, E. M. Kozulin, M. G. Itkis, G. N. Knyazheva, A. A. Bogachev, E. V. Chernysheva, L. Krupa, Yu. Ts. Oganessian, V. I. Zagrebaev, A. Ya. Rusanov, F. Goennenwein, O. Dorvaux, L. Stuttgé, F. Hanappe, E. Vardaci, and E. Goés de Brenand, “Fission and quasifission modes in heavy-ion-induced reactions leading to the formation of Hs^* ,” *Phys. Rev. C* **83**, 064613 (2011).
- [14] C. J. Lin, R. du Rietz, D. J. Hinde, M. Dasgupta, R. G. Thomas, M. L. Brown, M. Evers, L. R. Gasques, and M. D. Rodriguez, “Systematic behavior of mass distributions in ^{48}Ti -induced fission at near-barrier energies,” *Phys. Rev. C* **85**, 014611 (2012).

- [15] K. Nishio, S. Mitsuoka, I. Nishinaka, H. Makii, Y. Wakabayashi, H. Ikezoe, K. Hirose, T. Ohtsuki, Y. Aritomo, and S. Hofmann, “Fusion probabilities in the reactions $^{40,48}\text{Ca} + ^{238}\text{U}$ at energies around the Coulomb barrier,” *Phys. Rev. C* **86**, 034608 (2012).
- [16] C. Simenel, D. J. Hinde, R. du Rietz, M. Dasgupta, M. Evers, C. J. Lin, D. H. Luong, and A. Wakhle, “Influence of entrance-channel magicity and isospin on quasi-fission,” *Phys. Lett. B* **710**, 607–611 (2012).
- [17] R. du Rietz, E. Williams, D. J. Hinde, M. Dasgupta, M. Evers, C. J. Lin, D. H. Luong, C. Simenel, and A. Wakhle, “Mapping quasifission characteristics and timescales in heavy element formation reactions,” *Phys. Rev. C* **88**, 054618 (2013).
- [18] E. Williams, D. J. Hinde, M. Dasgupta, R. du Rietz, I. P. Carter, M. Evers, D. H. Luong, S. D. McNeil, D. C. Rafferty, K. Ramachandran, and A. Wakhle, “Evolution of signatures of quasifission in reactions forming curium,” *Phys. Rev. C* **88**, 034611 (2013).
- [19] A. Wakhle, C. Simenel, D. J. Hinde, M. Dasgupta, M. Evers, D. H. Luong, R. du Rietz, and E. Williams, “Interplay between Quantum Shells and Orientation in Quasifission,” *Phys. Rev. Lett.* **113**, 182502 (2014).
- [20] K. Hammerton, Z. Kohley, D. J. Hinde, M. Dasgupta, A. Wakhle, E. Williams, V. E. Oberacker, A. S. Umar, I. P. Carter, K. J. Cook, J. Greene, D. Y. Jeung, D. H. Luong, S. D. McNeil, C. S. Palshetkar, D. C. Rafferty, C. Simenel, and K. Stiefel, “Reduced quasifission competition in fusion reactions forming neutron-rich heavy elements,” *Phys. Rev. C* **91**, 041602(R) (2015).
- [21] E. Prasad, D. J. Hinde, K. Ramachandran, E. Williams, M. Dasgupta, I. P. Carter, K. J. Cook, D. Y. Jeung, D. H. Luong, S. McNeil, C. S. Palshetkar, D. C. Rafferty, C. Simenel, A. Wakhle, J. Khuyagbaatar, Ch. E. Düllmann, B. Lommel, and B. Kindler, “Observation of mass-asymmetric fission of mercury nuclei in heavy ion fusion,” *Phys. Rev. C* **91**, 064605 (2015).
- [22] E. Prasad, A. Wakhle, D. J. Hinde, E. Williams, M. Dasgupta, M. Evers, D. H. Luong, G. Mohanto, C. Simenel, and K. Vo-Phuoc, “Exploring quasifission characteristics for $^{34}\text{S} + ^{232}\text{Th}$ forming ^{266}Sg ,” *Phys. Rev. C* **93**, 024607 (2016).
- [23] G. G. Adamian, N. V. Antonenko, and W. Scheid, “Characteristics of quasifission products within the dinuclear system model,” *Phys. Rev. C* **68**, 034601 (2003).
- [24] Valery Zagrebaev and Walter Greiner, “Shell effects in damped collisions: a new way to superheavies,” *J. Phys. G* **34**, 2265 (2007).
- [25] Y. Aritomo, “Analysis of dynamical processes using the mass distribution of fission fragments in heavy-ion reactions,” *Phys. Rev. C* **80**, 064604 (2009).
- [26] Kai Zhao, Zhuxia Li, Yingxun Zhang, Ning Wang, Qingfeng Li, Caiwan Shen, Yongjia Wang, and Xizhen Wu, “Production of unknown neutron-rich isotopes in $^{238}\text{U} + ^{238}\text{U}$ collisions at near-barrier energy,” *Phys. Rev. C* **94**, 024601 (2016).
- [27] Takashi Nakatsukasa, Kenichi Matsuyanagi, Masayuki Matsuo, and Kazuhiro Yabana, “Time-dependent density-functional description of nuclear dynamics,” *Rev. Mod. Phys.* **88**, 045004 (2016).
- [28] Cédric Simenel, “Nuclear quantum many-body dynamics,” *Eur. Phys. J. A* **48**, 152 (2012).
- [29] J. W. Negele, “The mean-field theory of nuclear-structure and dynamics,” *Rev. Mod. Phys.* **54**, 913–1015 (1982).
- [30] Cédric Golabek and Cédric Simenel, “Collision Dynamics of Two ^{238}U Atomic Nuclei,” *Phys. Rev. Lett.* **103**, 042701 (2009).
- [31] David J. Kedziora and Cédric Simenel, “New inverse quasifission mechanism to produce neutron-rich transfermium nuclei,” *Phys. Rev. C* **81**, 044613 (2010).
- [32] V. E. Oberacker, A. S. Umar, and C. Simenel, “Dissipative dynamics in quasifission,” *Phys. Rev. C* **90**, 054605 (2014).
- [33] A. S. Umar, V. E. Oberacker, and C. Simenel, “Shape evolution and collective dynamics of quasifission in the time-dependent Hartree-Fock approach,” *Phys. Rev. C* **92**, 024621 (2015).
- [34] Kazuyuki Sekizawa and Kazuhiro Yabana, “Time-dependent Hartree-Fock calculations for multinucleon transfer and quasifission processes in the $^{64}\text{Ni} + ^{238}\text{U}$ reaction,” *Phys. Rev. C* **93**, 054616 (2016).
- [35] A. S. Umar, V. E. Oberacker, and C. Simenel, “Fusion and quasifission dynamics in the reactions $^{48}\text{Ca} + ^{249}\text{Bk}$ and $^{50}\text{Ti} + ^{249}\text{Bk}$ using a time-dependent Hartree-Fock approach,” *Phys. Rev. C* **94**, 024605 (2016).
- [36] Cédric Simenel, “Particle Transfer Reactions with the Time-Dependent Hartree-Fock Theory Using a Particle Number Projection Technique,” *Phys. Rev. Lett.* **105**, 192701 (2010).
- [37] Kazuyuki Sekizawa and Kazuhiro Yabana, “Time-dependent Hartree-Fock calculations for multinucleon transfer processes in $^{40,48}\text{Ca} + ^{124}\text{Sn}$, $^{40}\text{Ca} + ^{208}\text{Pb}$, and $^{58}\text{Ni} + ^{208}\text{Pb}$ reactions,” *Phys. Rev. C* **88**, 014614 (2013).
- [38] Kazuyuki Sekizawa and Kazuhiro Yabana, “Particle-number projection method in time-dependent Hartree-Fock theory: Properties of reaction products,” *Phys. Rev. C* **90**, 064614 (2014).
- [39] Kazuyuki Sekizawa, “Microscopic description of production cross sections including deexcitation effects,” *Phys. Rev. C* **96**, 014615 (2017).
- [40] Kazuyuki Sekizawa, “Enhanced nucleon transfer in tip collisions of $^{238}\text{U} + ^{124}\text{Sn}$,” *Phys. Rev. C* **96**, 041601(R) (2017).
- [41] C. H. Dasso, T. Dossing, and H. C. Pauli, “On the mass distribution in Time-Dependent Hartree-Fock calculations of heavy-ion collisions,” *Z. Phys. A* **289**, 395–398 (1979).
- [42] Cédric Simenel, “Particle-Number Fluctuations and Correlations in Transfer Reactions Obtained Using the Balian-Vénéroni Variational Principle,” *Phys. Rev. Lett.* **106**, 112502 (2011).
- [43] Y. Abe, S. Ayik, P.-G. Reinhard, and E. Suraud, “On stochastic approaches of nuclear dynamics,” *Phys. Rep.* **275**, 49 – 196 (1996).
- [44] R. Balian and M. Vénéroni, “Time-dependent variational principle for the expectation value of an observable: Mean-field applications,” *Ann. Phys.* **164**, 334 (1985).
- [45] E. Williams, K. Sekizawa, D. J. Hinde, C. Simenel, M. Dasgupta, I. P. Carter, K. J. Cook, D. Y. Jeung, S. D. McNeil, C. S. Palshetkar, D. C. Rafferty, K. Ramachandran, and A. Wakhle, “Exploring Zeptosecond Quantum Equilibration Dynamics: From Deep-Inelastic to Fusion-Fission Outcomes in $^{58}\text{Ni} + ^{60}\text{Ni}$ Reactions,” *Phys. Rev. Lett.* **120**, 022501 (2018).
- [46] H. Goutte, J. F. Berger, P. Casoli, and D. Gogny, “Microscopic approach of fission dynamics applied to fragment kinetic energy and mass distributions in ^{238}U ,” *Phys. Rev. C* **71**, 024316 (2005).
- [47] S. Ayik, “A stochastic mean-field approach for nuclear dynamics,” *Phys. Lett. B* **658**, 174 (2008).
- [48] M. Tohyama and A. S. Umar, “Quadrupole resonances in unstable oxygen isotopes in time-dependent density-matrix formalism,” *Phys. Lett. B* **549**, 72–78 (2002).
- [49] Marlène Assié and Denis Lacroix, “Probing Neutron Correlations through Nuclear Breakup,” *Phys. Rev. Lett.* **102**, 202501 (2009).
- [50] M. Tohyama and A. S. Umar, “Two-body dissipation effects on the synthesis of superheavy elements,” *Phys. Rev. C* **93**, 034607 (2016).

- (2016).
- [51] Denis Lacroix and Sakir Ayik, “Stochastic quantum dynamics beyond mean field,” *Eur. Phys. J. A* **50**, 95 (2014).
 - [52] Denis Lacroix, Sakir Ayik, and Bulent Yilmaz, “Symmetry breaking and fluctuations within stochastic mean-field dynamics: Importance of initial quantum fluctuations,” *Phys. Rev. C* **85**, 041602 (2012).
 - [53] Denis Lacroix, Danilo Gambacurta, and Sakir Ayik, “Quantal corrections to mean-field dynamics including pairing,” *Phys. Rev. C* **87**, 061302 (2013).
 - [54] Bulent Yilmaz, Denis Lacroix, and Resul Curebal, “Importance of realistic phase-space representations of initial quantum fluctuations using the stochastic mean-field approach for fermions,” *Phys. Rev. C* **90**, 054617 (2014).
 - [55] Yusuke Tanimura, Denis Lacroix, and Sakir Ayik, “Microscopic Phase-Space Exploration Modeling of ^{258}Fm Spontaneous Fission,” *Phys. Rev. Lett.* **118**, 152501 (2017).
 - [56] C. W. Gardiner, *Quantum Noise* (Springer-Verlag, Berlin, 1991).
 - [57] U. Weiss, *Quantum Dissipative Systems*, 2nd ed. (World Scientific, Singapore, 1999).
 - [58] Kouhei Washiyama, Sakir Ayik, and Denis Lacroix, “Mass dispersion in transfer reactions with a stochastic mean-field theory,” *Phys. Rev. C* **80**, 031602 (2009).
 - [59] B. Yilmaz, S. Ayik, D. Lacroix, and O. Yilmaz, “Nucleon exchange in heavy-ion collisions within a stochastic mean-field approach,” *Phys. Rev. C* **90**, 024613 (2014).
 - [60] S. Ayik, B. Yilmaz, and O. Yilmaz, “Multinucleon exchange in quasifission reactions,” *Phys. Rev. C* **92**, 064615 (2015).
 - [61] S. Ayik, O. Yilmaz, B. Yilmaz, and A. S. Umar, “Quantal nucleon diffusion: Central collisions of symmetric nuclei,” *Phys. Rev. C* **94**, 044624 (2016).
 - [62] S. Ayik, B. Yilmaz, O. Yilmaz, A. S. Umar, and G. Turan, “Multinucleon transfer in central collisions of $^{238}\text{U} + ^{238}\text{U}$,” *Phys. Rev. C* **96**, 024611 (2017).
 - [63] A. S. Umar, M. R. Strayer, J. S. Wu, D. J. Dean, and M. C. Güçlü, “Nuclear Hartree-Fock calculations with splines,” *Phys. Rev. C* **44**, 2512–2521 (1991).
 - [64] A. S. Umar and V. E. Oberacker, “Three-dimensional unrestricted time-dependent Hartree-Fock fusion calculations using the full Skyrme interaction,” *Phys. Rev. C* **73**, 054607 (2006).
 - [65] E. Chabanat, P. Bonche, P. Haensel, J. Meyer, and R. Schaeffer, “A Skyrme parametrization from subnuclear to neutron star densities Part II. Nuclei far from stabilities,” *Nucl. Phys. A* **635**, 231–256 (1998).
 - [66] Ka-Hae Kim, Takaharu Otsuka, and Paul Bonche, “Three-dimensional TDHF calculations for reactions of unstable nuclei,” *J. Phys. G* **23**, 1267 (1997).
 - [67] W. U. Schröder, J. R. Huizenga, and J. Randrup, “Correlated mass and charge transport induced by statistical nucleon exchange in damped nuclear reactions,” *Phys. Lett. B* **98**, 355–359 (1981).
 - [68] A. C. Merchant and W. Nörenberg, “Neutron and proton diffusion in heavy-ion collisions,” *Phys. Lett. B* **104**, 15–18 (1981).
 - [69] Hannes Risken and Till Frank, *The Fokker-Planck Equation* (Springer-Verlag, Berlin, 1996).
 - [70] W. Nörenberg, “Memory effects in the energy dissipation for slow collective nuclear motion,” *Phys. Lett. B* **104**, 107–111 (1981).
 - [71] J. Randrup, “Theory of transfer-induced transport in nuclear collisions,” *Nucl. Phys. A* **327**, 490–516 (1979).
 - [72] A. C. Merchant and W. Nörenberg, “Microscopic transport theory of heavy-ion collisions,” *Z. Phys. A* **308**, 315–327 (1982).
 - [73] K. Gottfried, *Quantum Mechanics* (W. A. Benjamin Inc., New York, 1966).